INORGANIC CHEMISTRY FRONTIERS

REVIEW

View Article Online
View Journal | View Issue

Cite this: *Inorg. Chem. Front.*, 2024, **11**, 5004

A dual-heteroatom–lanthanide cluster-embedded polyoxotungstate for sequential fluorescence detection of Fe^{3+} and pyrophosphate†

Siyu Zhang,‡[a,b] Tiantian Gong,‡[b] Chenyun Liu,[a,b] Qiuyu Wang,[b] Fuxiu Chen,[b] Jiancai Liu,*[a,b] Lijuan Chen*[b] and Junwei Zhao *[a,b]

A neoteric inorganic–organic hybrid dual-heteroatom (HA) and lanthanide (Ln) cluster-bridged polyoxotungstate (POT) $[H_8BTHMMAP]_{1.5}[H_2N(CH_3)_2]_4Na_3H[Eu_2Bi_3(Hpdca)_3(H_2O)_3Te_2W_3O_{14}][(W_5O_{18})(B\text{-}\alpha\text{-}BiW_9O_{33})_2]\cdot 44H_2O$ (**1**, $H_6BTHMMAP$ = 1,3-bis[tris-(hydroxymethyl)methylamino]propane, Hpdca = 2-pyridinic acid) was prepared by the dual-HA template strategy. The skeleton of **1** possesses a three-bladed propeller-shaped $[Eu_2Bi_3(Hpdca)_3(H_2O)_3Te_2W_3O_{14}]^{13+}$ core wrapped by two Keggin $[B\text{-}\alpha\text{-}BiW_9O_{33}]^{9-}$ and one Lindqvist $[W_5O_{18}]^{6-}$ segments. Noteworthily, the intricate $[Eu_2Bi_3(Hpdca)_3(H_2O)_3Te_2W_3O_{14}]^{13+}$ unit consisting of a Bi–Te dual-HA-bridged Ln–W polynuclear cluster is rather attractive and rarely seen in POT crystal engineering. Prominently, **1** exhibits an "ON–OFF" luminescence response triggered by Fe^{3+} based on dynamic quenching and competitive absorption, and the subsequent addition of pyrophosphate (PPi) leads to the recovery of luminescence due to the efficient interaction of Fe^{3+} and PPi. The developed "ON–OFF–ON" switch allows the consecutive discrimination of Fe^{3+} and PPi with low detection limits of 1.23 μM and 2.16 μM, respectively. This work provides a profound understanding of the dual-HA template approach in assembling complicated POTs, and shows the great potential of POT materials in environmental and biological detection.

Received 19th April 2024,
Accepted 16th June 2024

DOI: 10.1039/d4qi00991f

rsc.li/frontiers-inorganic

Introduction

The template strategy with the ingenious use of anions to achieve selective assembly has emerged as a versatile and valuable route to discover new reaction phenomena and access intricate molecular structures.[1–6] A large number of examples have demonstrated that the template strategy can promote the ordered arrangement of building blocks (BBs) around them and is critical in influencing the overall architectures (nuclearity, size, and geometry) and physicochemical properties (stability, redox properties, acidity, *etc.*).[1–9] Heteropolyoxotungstates (HPOTs) are a class of heteroatom (HA)-templated metal oxides and have been extensively applied in luminescence, catalysis, medicine, magnetism, materials science, *etc.*[10–15] Within HPOTs, HA species are wide ranging (from III to VI main groups such as B^{III}, Si^{IV}, Ge^{IV}, $P^{III/V}$, $As^{III/V}$, Sb^{III}, Bi^{III}, Se^{IV} and Te^{IV}), and the combination of diverse HA templates with tungstates leads to a large library of extraordinary HPOTs,[16–20] denoting a versatile subclass of the polyoxometalate (POM) family.

Apart from the common function of HAs as interior structure-directing templates for generating BBs to capture metal ions [transition metal (TM) or lanthanide (Ln)], they can also work as extra linkers to control metal or inter-cluster aggregation.[21–32] For example, Cronin *et al.* isolated a series of gigantic pure HPOTs $[(H_8W_{100}Se_{16}O_{364})WO(H_2O)_2]^{52-}$ (Fig. S1a†), $[W_{28}Te_8O_{112}]^{24-}$, $[W_{28}Te_9O_{115}]^{26-}$ and $[W_{28}Te_{10}O_{118}]^{28-}$, where the *in situ*-formed $[Se_3W_{25}O_{91}]^{20-}$ or $[TeW_7O_{28}]^{8-}$ BBs are connected by additional Se^{IV} or Te^{IV} linkers.[23,24] Later, Wang *et al.* showed the effectiveness of P^V linkers in gathering Co^{2+} ions for the formation of the high-nuclear-Co^{2+} substituted HPOT $[\{Co_4(OH)_3(PO_4)\}_4(PW_9O_{34})_4]^{28-}$ (Fig. S1b†).[26] Noteworthily, besides the discrete HA linkers, the HA cluster linkers utilized for constructing HPOT BBs have also been discovered.[27–32] For instance, Long and Kong *et al.* obtained a heterometallic tetramer $[Ln_3(H_2O)_5Ni(H_2O)_3(Sb_4O_4)(SbW_9O_{33})_3(NiW_6O_{24})(WO_2)_3(CH_3COO)]^{17-}$ (Ln = La^{3+}, Pr^{3+}, Nd^{3+}) (Fig. S1c†), featuring three $[SbW_9O_{33}]^{9-}$ and one

[a]*School of Energy Science and Technology, Henan University, Zhengzhou, Henan 450046, People's Republic of China. E-mail: liujiancai@henu.edu.cn*
[b]*Henan Key Laboratory of Polyoxometalate Chemistry, College of Chemistry and Molecular Sciences, Henan University, Kaifeng, Henan 475004, People's Republic of China. E-mail: ljchen@henu.edu.cn, zhaojunwei@henu.edu.cn*

†Electronic supplementary information (ESI) available: Experimental section, crystal data, additional figures and tables. CCDC 2335445. For ESI and crystallographic data in CIF or other electronic format see DOI: https://doi.org/10.1039/d4qi00991f

‡Si-Yu Zhang and Tian-Tian Gong contributed equally to this work.

$[Ni^{II}W_9O_{33}]^{10-}$ BB linked by a tetrahedral $[Sb_4O_4]$-connected metal core $[Ln_3(H_2O)_5Ni(H_2O)_3(Sb_4O_4)(CH_3COO)]^{14+}$.[29] Recently, Zheng *et al.* have reported a POM species $[Sb_{15}Tb_7W_3O_{29}(OH)_3(DMF)(H_2O)_6(SbW_8O_{30})(SbW_9O_{33})_5]^{27-}$ with the highest-nuclear $Sb^{III/V}$ centers, in which the Sb-rich cluster cores contain dimeric $\{Sb_2O_6\}$ and $\{Sb_2O_7\}$, trimeric $\{Sb_3O_{10}\}$ and pentameric $\{Sb_5O_{12}(OH)\}$ linkers (Fig. S1d†).[30] Besides, Bi^{III} cluster linkers generally in the form of $\{Bi_6O_x\}$ were also used to obtain Ln^{3+} ions and BBs, which have been previously seen in HPOTs such as $[(BiW_9O_{33})_4(WO_3)\{Bi_6(\mu_3\text{-}O)_4(\mu_2\text{-}OH)_3\}(Ln_3(H_2O)_6CO_3)]^{22-}$ (Fig. S1e†) and $\{[W_{14}Ce^{IV}_6O_{61}]([W_3Bi_6Ce^{III}_3(H_2O)_3O_{14}][B\text{-}\alpha\text{-}BiW_9O_{33}]_3)_2\}^{34-}$ (Fig. S1f†).[31,32]

Based on these innovative works, particular attention has been paid to the designed fabrication of novel HPOTs by judiciously choosing mixed-HA components. In principle, the synergetic assembly of two or more types of HAs can not only give access to novel HPOTs with diverse architectures, but also provide a great opportunity for generating novel BBs or functionalities. Hitherto, some unprecedented dual-HA-directed HPOTs have been synthesized by reasonably selecting HA pairs.[33–43] However, those reported species are generally predominated by one kind of HA linker, and those with two kinds of HA linkers remain underexplored. Therefore, exploring mixed-HA-bridged HPOTs is still a challenging task.

In this work, a multicomponent self-assembly system by applying two kinds of HA materials (K_2TeO_3 and $Bi(NO_3)_3{\cdot}5H_2O$) to react with tungstates and Ln ions in the presence of organic components (1,3-bis[tris(hydroxymethyl) methylamino]propane ($H_6BTHMMAP$), 2-pyridinic acid (Hpdca), and dimethylamine hydrochloride) in acidic aqueous medium was established. The selection of Te^{IV} and Bi^{III} HAs is largely due to their flexibility in structural regulation and ease of crystallographical differentiability. To be specific, the lone-electron-pair stereochemical effect of Te^{IV} and Bi^{III} HAs can to some extent impede the closure of *in situ*-generated BBs. Another reason is that they can work as bridges individually or together to integrate Ln centers or BBs into larger aggregates. In terms of organic ligands, the polydentate $H_6BTHMMAP$ and Hpdca molecules with flexible N and O binding sites are excellent synthons as potential chelating and bridging units by coordinating N or O donors to Ln or W centers, which can effectively control Ln hydrolysis. The protonated species of organic molecules can also serve as countercations. With this strategy, an inorganic–organic Hpdca-ornamented dual-HA–Ln cluster-bridged HPOT trimer $[H_8BTHMMAP]_{1.5}[H_2N(CH_3)_2]_4Na_3H[Eu_2Bi_3(Hpdca)_3(H_2O)_3Te_2W_3O_{14}][(W_5O_{18})(B\text{-}\alpha\text{-}BiW_9O_{33})_2]{\cdot}44H_2O$ (**1**) was achieved. Polyanion **1** is composed of two $[B\text{-}\alpha\text{-}BiW_9O_{33}]^{9-}$ and one $[W_5O_{18}]^{6-}$ BBs unified by one neoteric decanuclear heterometallic $[Eu_2Bi_3(Hpdca)_3(H_2O)_3Te_2W_3O_{14}]^{13+}$ cluster, which represents an extremely rare case that contains mixed HA cluster linkers in POM chemistry. **1** was preliminarily characterized by infrared (IR) and thermogravimetric (TG) analyses (Fig. S2 and S3†), and the powder X-ray diffraction (PXRD) analysis confirmed the good phase purity of **1** (Fig. S4†). Furthermore, an "ON–OFF–ON" system was proposed by developing **1** as a luminescent probe for the sensitive and selective detection of Fe^{3+} and pyrophosphate ($P_2O_7^{4-}$, PPi) in an aqueous environment. Specifically, the emission of **1** was significantly quenched by Fe^{3+} owing to the dynamic quenching and competitive absorption, while the selective binding effect of PPi with Fe^{3+} could gradually restore the luminescence with a recovery rate of about 78%. Such a probe can be practically employed in water and serum sample analyses.

Results and discussion

Structural description

1 crystallizes in the monoclinic space group $P21/c$ (Table S1†) and its molecular skeleton comprises a trimeric polyoxoanion $[Eu_2Bi_3(Hpdca)_3(H_2O)_3Te_2W_3O_{14}][(W_5O_{18})(B\text{-}\alpha\text{-}BiW_9O_{33})_2]^{11-}$ (**1a**). **1a** displays a triangular arrangement of two trivacant Keggin $[B\text{-}\alpha\text{-}BiW_9O_{33}]^{9-}$ ($\{BiW_9\}$) BBs and one monovacant Lindqvist $[W_5O_{18}]^{6-}$ ($\{W_5\}$) BB connected by an intriguing three-bladed "propeller-shaped" $[Eu_2Bi_3(Hpdca)_3(H_2O)_3Te_2W_3O_{14}]^{13+}$ ($\{Eu_2Bi_3(Hpdca)_3Te_2W_3\}$) cluster (Fig. 1a, e and f). As exhibited in Fig. 1a, **1a** can be viewed as one $\{W_5\}$ BB capped on a dimeric $[Eu_2Bi_3(Hpdca)_3(H_2O)_3Te_2W_3O_{14}][(B\text{-}\alpha\text{-}BiW_9O_{33})_2]^{5-}$ fragment, where the $Eu1^{3+}$ ion in $\{Eu_2Bi_3(Hpdca)_3Te_2W_3\}$ is just inserted into the vacant position of $\{W_5\}$ BB and two metal–organic $[Bi(Hpdca)]^{3+}$ (Bi4 and Bi5) cations simultaneously work as connectors to link one $\{W_5\}$ and two $\{BiW_9\}$ BBs (Fig. 1a and b), producing four Eu–O–W and two Bi–O–W bonds to reinforce the structural stability of **1a**. Remarkably, in the $[Eu_2Bi_3(Hpdca)_3(H_2O)_3Te_2W_3O_{14}][(B\text{-}\alpha\text{-}BiW_9O_{33})_2]^{5-}$ dimer, one peculiar dual-HA-participated multi-nuclear $[EuBi_2(Hpdca)_2(H_2O)_2Te_2O_5]^{7+}$ cluster is anchored onto the "open" $[EuBi(Hpdca)(H_2O)W_3O_9][(B\text{-}\alpha\text{-}BiW_9O_{33})_2]^{12-}$ dimeric midbody by coordinating two Bi^{III} ($Bi4^{III}$, $Bi5^{III}$) and two Te^{IV} ($Te1^{IV}$, $Te2^{IV}$) atoms with four terminal-O (O_t) atoms from two $\{BiW_9\}$ BBs as well as coordinating two Te^{IV} ($Te1^{IV}$, $Te2^{IV}$) atoms and one $Eu1^{3+}$ ion with three vertex O2, O1 and O25 atoms from one bridging $\{WO_6\}$ octahedron (Fig. 1b and c). For the $[EuBi(Hpdca)(H_2O)W_3O_9][(B\text{-}\alpha\text{-}BiW_9O_{33})_2]^{12-}$ fragment, it can be explicitly observed that two $\{BiW_9\}$ BBs are firstly interlinked by one $[Eu2(Hpdca)]^{3+}$ unit *via* four O_t atoms (O33, O41, O17, O56) into an open $[Eu(Hpdca)][(B\text{-}\alpha\text{-}BiW_9O_{33})_2]^{15-}$ dimer, followed by the accommodation of one $[BiW_3(H_2O)O_{11}]^-$ BB *via* four Bi–O_t–W (O_t: O23, O41, O9, O56) and four W–O_t–W (O23, O54, O9, O20) bonds (Fig. 1c, d and S5†).

A prominent characteristic of **1a** is the intricate three-bladed propeller-shaped $\{Eu_2Bi_3(Hpdca)_3Te_2W_3\}$ core (Fig. 1f). Interestingly, three Hpdca ligands, like blades, are aligned in three different directions around the "propeller shaft" $[Eu_2Bi_3(H_2O)_3Te_2W_3O_{14}]^{13+}$ ($\{Eu_2Bi_3Te_2W_3\}$) cluster (Fig. 1g) by fixing to Eu2, Bi4 and Bi5 atoms through N and carboxyl-O sites, giving rise to two five-membered "–Eu–O–C–C–N–" and "–Bi–O–C–C–N–" rings (Fig. 1h). Noticeably, the phenomenon of Hpdca ligands in tethering with the Bi atom is rarely encountered. $\{Eu_2Bi_3Te_2W_3\}$ can be viewed as a combination

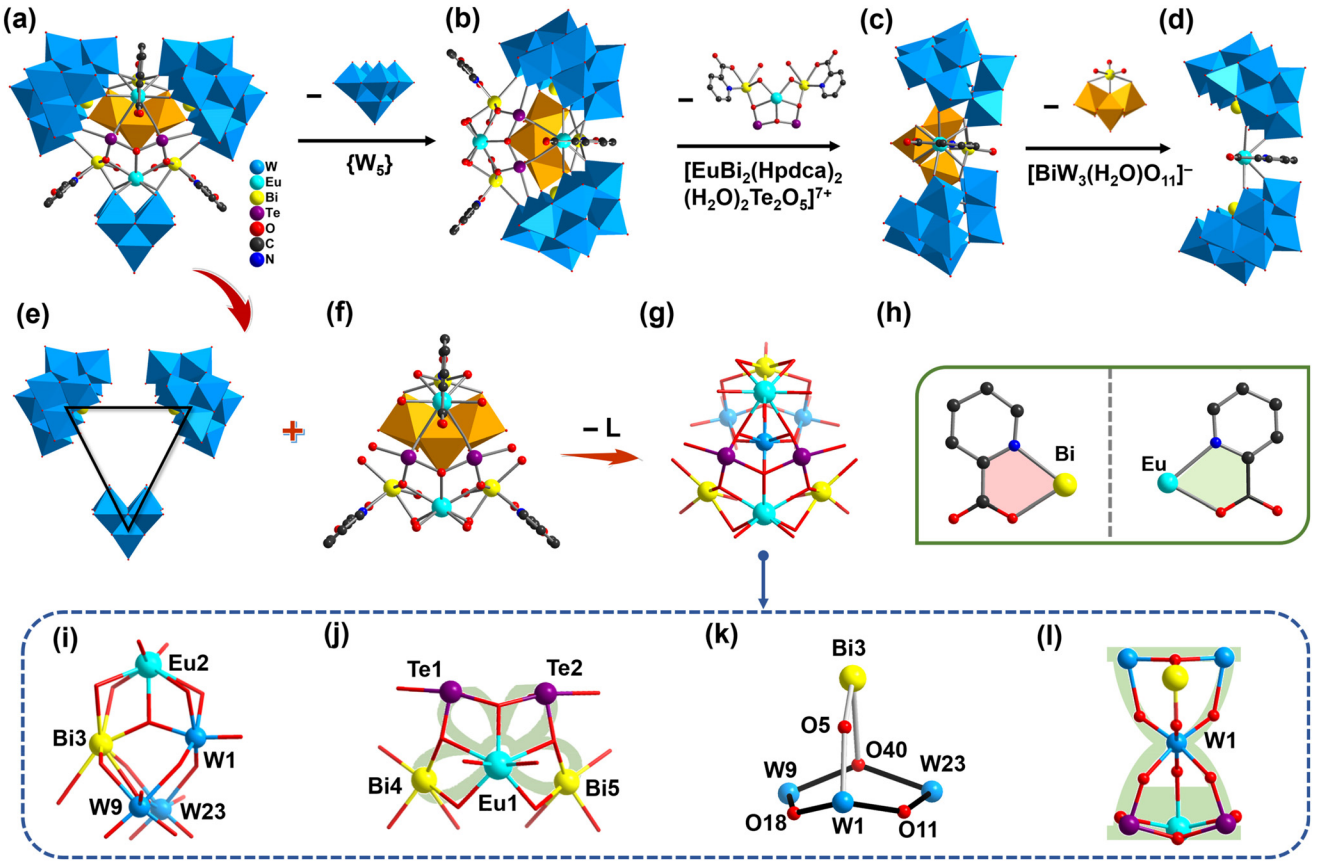

Fig. 1 (a) The structure of **1a**. (b) The $[Eu_2Bi_3(Hpdca)_3(H_2O)_3Te_2W_3O_{14}][(B\text{-}\alpha\text{-}BiW_9O_{33})_2]^{5-}$ fragment formed by removing the $\{W_5\}$ BB from **1a**. (c) The $[EuBi(Hpdca)(H_2O)W_3O_9][(B\text{-}\alpha\text{-}BiW_9O_{33})_2]^{12-}$ fragment formed by removing one $[EuBi_2(Hpdca)_2(H_2O)_2Te_2O_5]^{7+}$ cluster from the $[Eu_2Bi_3(Hpdca)_3(H_2O)_3Te_2W_3O_{14}][(B\text{-}\alpha\text{-}BiW_9O_{33})_2]^{5-}$ dimer. (d) The $[Eu(Hpdca)][(B\text{-}\alpha\text{-}BiW_9O_{33})_2]^{15-}$ fragment formed by removing one $[BiW_3(H_2O)O_{11}]^-$ BB from the $[EuBi(Hpdca)(H_2O)W_3O_9][(B\text{-}\alpha\text{-}BiW_9O_{33})_2]^{12-}$ fragment. (e) The arrangement of two $\{BiW_9\}$ and one $\{W_5\}$ subunits showing the triangular motif. (f) The three-bladed "propeller-shaped" $\{Eu_2Bi_3(Hpdca)_3Te_2W_3\}$ cluster. (g) The $\{Eu_2Bi_3Te_2W_3\}$ cluster by removing three Hpdca ligands, where L represents the Hpdca ligand. (h) Two five-membered "–Bi–O–C–C–N–" and "–Eu–O–C–C–N–" rings. (i) and (j) The $[EuBi(H_2O)W_3O_{10}]^{4+}$ and $[EuBi_2(H_2O)_2Te_2O_4]^{9+}$ fragments constituting the $\{Eu_2Bi_3Te_2W_3\}$ cluster. (k) The $\{BiW_3O_4\}$ fragment showing the bridged hydrocarbon-shaped geometry. (l) The "hourglass-shaped" $[EuBiW_3(H_2O)Te_2O_{14}]^{4+}$ fragment.

of $[EuBi(H_2O)W_3O_{10}]^{4+}$ and $[EuBi_2(H_2O)_2Te_2O_4]^{9+}$ clusters (Fig. 1i and j). In the $[EuBi(H_2O)W_3O_{10}]^{4+}$ cluster, the $[BiW_3(H_2O)O_{11}]^-$ BB comprises three vertex-shared $\{WO_6\}$ octahedra in a triangle motif, in which Bi3 and W1 atoms are ligated to the Eu2 atom *via* five O atoms (Fig. 1i). Besides, a unique octa-membered $\{BiW_3O_4\}$ segment with a novel bridged hydrocarbon-shaped geometry such as bicyclo[2,2,2]-octane was noticed in $[BiW_3(H_2O)O_{11}]^-$ BB (Fig. 1k), quite distinct from the well-known cubane structure. The $[EuBi_2(H_2O)_2Te_2O_4]^{9+}$ cluster comprises a centric Eu1 atom surrounded by outward two Te and two Bi atoms in the order of "Bi4–Te1–Te2–Bi5" *via* five O bridges, and each Te or Bi atom is in conjunction with the Eu1 atom by sharing two μ_3-O atoms, generating a petal-like motif with one side opening (Fig. 1g). This arrangement also gives rise to a folded $[EuTe_2O_3]^{5+}$ quadrangle along the "Eu1–O3" line (Fig. S6†). Actually, two Te and two Bi atoms are almost coplanar to build a trapezoid plane whereas the Eu1 atom is located above the plane with a distance of 1.992 Å (Fig. S7†). A close inspection into the $\{Eu_2Bi_3Te_2W_3\}$ cluster unveils a peculiar "hourglass-shaped" $[EuBiW_3(H_2O)Te_2O_{14}]^{4+}$ fragment based on $[BiW_3(H_2O)O_{11}]^-$ BB and $[EuTe_2O_3]^{5+}$ section, which can be reasonably divided into the upper $\{BiW_3O_4\}$ and the lower $\{EuTe_2O_6\}$ parts sharing one middle W1 atom (Fig. 1j).

Noteworthily, five crystallographically independent Bi^{III} atoms in a **1a** polyoxoanion play two roles: $Bi1^{III}$ and $Bi2^{III}$ atoms as templates are embedded in $\{BiW_9\}$ BBs while $Bi3^{III}$–$Bi5^{III}$ atoms as linkers are situated between BBs. In particular, $Bi3^{III}$–$Bi5^{III}$ linkers are involved in different binding environments: the $Bi3^{III}$ atom is surrounded by seven O-coordinate spheres with four from two adjacent $\{BiW_9\}$ BBs, two from the $\{BiW_3\}$ BB, and one from the water ligand (Fig. S8†); $Bi4^{III}$ and $Bi5^{III}$ atoms are coordinated by Hpdca ligands *via* N and carboxyl O sites and then encircled by two O_t atoms from $\{BiW_9\}$ and $\{W_5\}$ BBs, one μ_3-O atom from the $[EuTe_2O_3]^{5+}$ fragment and one from the water ligand, both displaying the hexa-coordinate configuration (Fig. S8†). Three Bi^{III} linkers have an average Bi–O and Bi–N bond lengths of 2.421 and 2.372 Å, and

the Bi–O bond lengths are a bit longer than those in BBs (2.133 Å). Both Te^{IV} atoms play the bridging role and are in a four-coordinate geometry defined by two, one and one O atoms from $[EuTe_2O_3]^{5+}$, $[BiW_3(H_2O)O_{11}]^-$ and {BiW_9} BBs with Te–O distances of 1.857(8)–2.223(9) Å (Fig. S9†). The $Eu1^{3+}$ ion displays the octa-coordinate bicapped triangular prism geometry completed by four O_t atoms from the {W_5} BBs, three μ_3-O atoms from the $[EuTe_2O_3]^{5+}$ fragment and one μ_2-O atom from the $[BiW_3(H_2O)O_{11}]^-$ BBs, whilst the $Eu2^{3+}$ ion adopts a nona-coordinate mono-capped square antiprism geometry defined by four O_t atoms from two {BiW_9} BBs, three μ_3-O atoms from the {$W1O_6$} octahedron as well as one carboxyl O and N atoms from the Hpdca ligand (Eu–O: 2.277(9)–2.776(9) Å) (Fig. S10†).

In the stacking diagram, trimeric **1a** polyoxoanions are packed together to form an interesting supra-molecular architecture through intermolecular interactions, where the charge compensating cations ($[H_8BTHMMAP]^{2+}$, $[H_2N(CH_3)_2]^+$, H^+ and Na^+) and water molecules fill in the pores among **1a** polyoxoanions. For clarity, countercations and water molecules are omitted, and the stacking framework along the *c* axis reveals that neighboring layers (named layer A and B) are stacked in an –ABAB– sequence (Fig. S11†). Hereinto, two adjacent **1a** polyoxoanions are intersected and distributed in a "face-to-face" pattern, constituting a repeating unit in each layer. Unlike the "back–front" order of two **1a** polyoxoanions in the repeating unit in layer A, the **1a** polyoxoanion in layer B shows a converse "back–front" order. The simplified graph by visualizing **1a** as a triangle (built by Bi1, Bi2 and W15 atoms) makes us more clearly understand the arrangement of **1a** polyoxoanions (Fig. S11†).

Stability studies of 1a in solution

The stability of **1a** in water was explored by electrospray ionization mass spectrometry (ESI-MS) in negative mode and UV-vis absorption spectra. As shown in Fig. S12 and Table S2,† there are three groups of charged peaks with negative charges of 6– (*m*/*z* values: 1364.31, 1410.49, 1457.82), 5– (*m*/*z* values: 1680.28, 1755.27) and 4– (*m*/*z* values: 2151.93, 2203.94). The peak at *m*/*z* 1364.31 can be assigned to $\{[H_2N(CH_3)_2]_2Na_3[Eu_2Bi_3(H_2O)_4Te_2W_3O_{14}][(W_5O_{18})(BiW_9O_{33})_2]\}^{6-}$, implying that three Hpdca ligands are released from **1a**. The remaining peaks correspond to the species of $[Eu_2Bi_3(Hpdca)_3(H_2O)_nTe_2W_3O_{14}][(W_5O_{18})(BiW_9O_{33})_2]^{11-}$ polyanions with different numbers of counter cations ($[H_2N(CH_3)_2]^+$, H^+, $[H_8BTHMMAP]^{2+}$, or Na^+). These results corroborate that the skeleton of **1a** is basically stable in water. By extending time, the first two groups (*m*/*z* values less than 2000) of signal peaks gradually weakened while the third group (*m*/*z* values between 2000–2400) gradually disappeared at 24 h (Fig. 2a). By contrast, **1a** is more sensitive to pH because partial peaks have completely vanished when pH is lower than 3.3 or higher than 9.3 (Fig. 2b). Besides, UV-vis spectra were also recorded to explore its stability in water. Evidently, one strong absorption band at 192 nm and one weak absorption band around 260 nm were observed, respectively corresponding to $O_t \rightarrow W$ and $O_{b(c)} \rightarrow W$ pπ–dπ charge-transfer transitions. Notably, the UV-vis spectra of **1** didn't show obvious changes by prolonging time to 24 h, indicating that **1a** is basically stable for 24 h (Fig. 2c). However, the intensity of $O_{b(c)} \rightarrow W$ and $O_t \rightarrow W$ bands slowly shifted and decreased when the pH is out of the 3–10 range, as revealed in pH-dependent UV-vis spectra (Fig. 2d). Overall, the UV-vis result basically matches with ESI-MS data. Thus, the structural stability of **1a** can be maintained for 24 h, or in the pH range of 3.3–8.3.

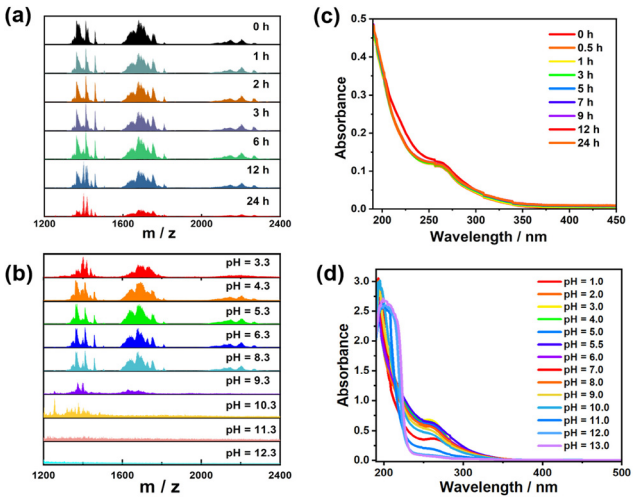

Fig. 2 (a) Time-dependent ESI-MS spectra of **1** in water. (b) The pH-dependent ESI-MS spectra of **1** in water. (c) Time-dependent UV-vis spectra of **1** in water. (d) The pH-dependent UV-vis spectra of **1** in water.

Photoluminescence (PL) sensing properties

Ferric ion (Fe^{3+}) is an essential trace element for the human body, and is also an important component of hemoglobin, many enzymes and immune system compounds.[44–46] However, the abnormalities of Fe^{3+} in the human body can lead to various diseases such as anemia, renal failure, liver damage and hemochromatosis. In addition, an excess of Fe^{3+} threatens the ecological environment.[47,48] Hence, the detection of Fe^{3+} is vital to the early warning of underlying diseases or environmental damage. Among the diverse detection strategies, PL sensing methods have aroused great interest owing to their high selectivity and sensitivity, convenient operation, and low sample consumption. As a water-stable and easy-to-prepare Eu-based PL material, **1** could be developed as a probe to detect Fe^{3+}.

Motivated by this idea, the PL behaviors of **1** in water were studied. Five well-resolved emission peaks at 578, 594, 620, 654 and 699 nm were observed in the spectrum of **1** (2 mg mL^{-1}) that can be identified as the $^5D_0 \rightarrow {}^7F_J$ (J = 0–4) transitions of Eu^{3+} ions upon excitation at 397 nm (Fig. S13a†).[49,50] The $^5D_0 \rightarrow {}^7F_2$ transition at 620 nm is dominated by a splitting peak at 618 nm. Monitored at the strongest emission, the excitation spectrum of **1** exhibits one broad band at around 350 nm attributed to the O → W charge transfer of {BiW_9} and {W_5} BBs, as well as five typical peaks at 363 nm ($^7F_0 \rightarrow {}^5D_4$), 383 nm ($^7F_0 \rightarrow {}^5G_2$), 397 nm ($^7F_0 \rightarrow {}^5L_6$), 418 nm ($^7F_0 \rightarrow {}^5D_3$)

and 467 nm ($^7F_0 \rightarrow {}^5D_2$) from Eu^{3+} ions (Fig. S13b†). Additionally, the decay lifetime of **1** under the 397 nm excitation peak and 620 nm emission peak can be calculated as 816.04 μs by fitting with the mono-exponential function $I = A\exp(-t/\tau_1)$ (Fig. S13c†), where A represents pre-exponential factor and τ_1 represents the luminescence lifetime. Moreover, the time-dependent PL emission of **1** (2 mg mL^{-1}) in water was studied (Fig. S14†). The intensity shows a slow attenuation that may be caused by dynamic exchange between water molecules in **1** and solution, and a total decrease of 9% within 10 h at 620 nm indicates the PL emission of **1** is basically stable in water for a long time.

Based on the excellent PL behavior in water, sensing experiments were carried out by employing **1** (2 mg mL^{-1}) as a probe. As revealed in Fig. 3a, the emission evolution of **1** towards Fe^{3+} triggers an "ON–OFF" response as the emission intensity gradually decreases to approximately 26% with the concentration of Fe^{3+} ranging from 0 to 400 μM. Additionally, a good linear Stern–Volmer (S–V) function fitted by $I_0/I = 0.992 + 0.00218[C_{Fe}]$ with a correlation coefficient (R^2) of 0.994 was obtained between intensity ratio (I_0/I, I_0 and I represent the emission intensity without or with the addition of Fe^{3+}) at 620 nm and Fe^{3+} concentration ($[C_{Fe}]$, 0–150 μM) (Fig. 3b), implying that the quantitative detection of Fe^{3+} by **1** is applicable over a wide $[C_{Fe}]$ range. As $[C_{Fe}]$ continues to increase, the fitting curve gradually deviates from linearity and bends upward, which can be perfectly fitted by an exponential function. The limit of detection (LOD) was determined to be 1.23 μM based on the definition of LOD = $3s/k$, where s indicates the standard deviation of three blank tests, and k is the slope of the linear fitting curve (Table S3†).[51] This LOD value is apparently lower than the permissible limit of Fe^{3+} in drinking water given by the World Health Organization (WHO) (5.37 μM).

By comparison, other cations $M(Cl)_x$ (M^{x+} = Na^+, K^+, Li^+, Mg^{2+}, Ca^{2+}, Al^{3+}, and Cd^{2+}) or anions Na_xN (N^{x-} = CH_3COO^-, NO_3^-, $H_2PO_4^-$, and SO_4^{2-}) with the same concentration of 400 μM can hardly quench **1** (Fig. S15†). Furthermore, hierarchical cluster analysis (HCA) was applied for classifying analytes, which was calculated by the HCA algorithm based on PL intensity at 620 nm. Evidently, Fe^{3+} can be completely recognized from other ions from the root node of the clustering tree (Fig. 3c). Fig. 3d also shows the distance of HCA between ions where blue suggests they are far away and red suggests that they are close. The coexistence of interfering species with Fe^{3+} led to minor or negligible effects on the emission intensity (Fig. 3e), indicative of the remarkable anti-interference ability of **1** towards the determination of Fe^{3+}. The excellent detection performances of **1** drive us to evaluate its potential utility in actual samples. A series of lake water, tap water and human serum samples were filtered and spiked with various amounts of Fe^{3+} by standard addition method. And Fe^{3+} concentration in the above samples was computed by PL intensity tests and compared with the actual amount added. As manifested in Table S4,† the recoveries of 99.19%–100.50% with a relative standard deviation (RSD) of 0.83%–1.82% in tap water,

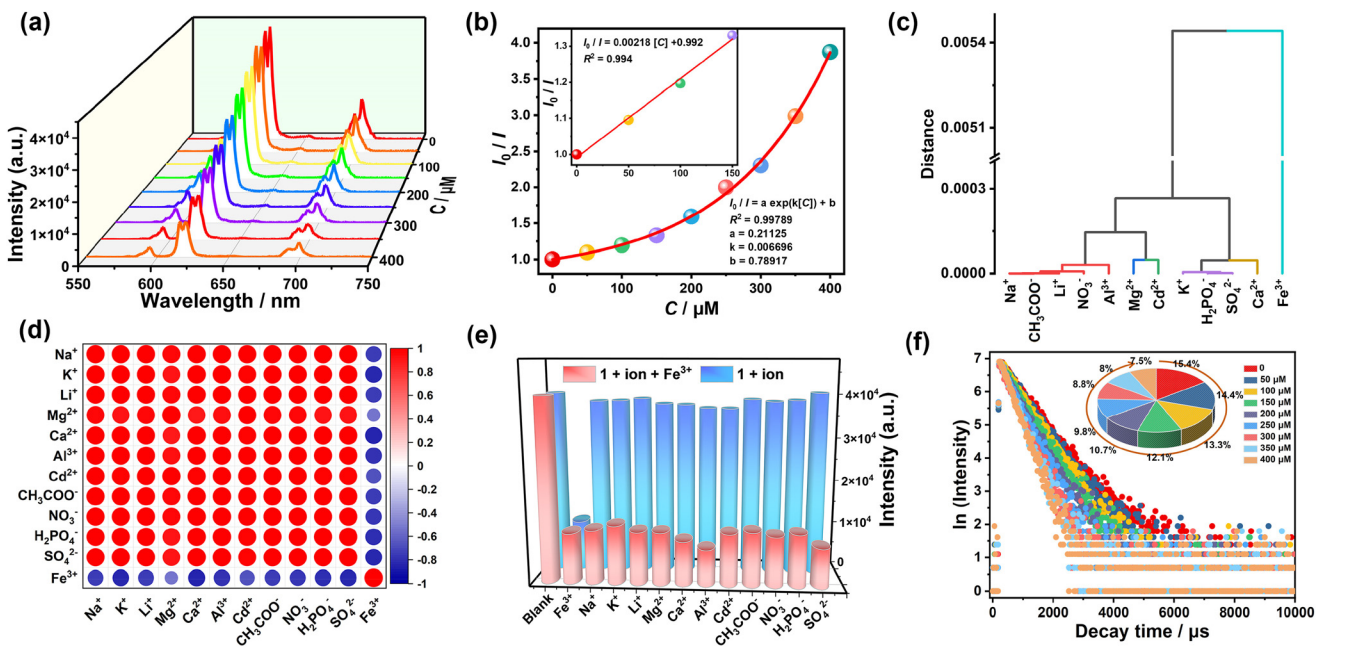

Fig. 3 (a) Evolution of the emission spectra of the **1**-based sensor with different concentrations of Fe^{3+}. (b) Plot of PL intensity ratio *vs.* the concentrations of Fe^{3+}. Inset: the linear variation of I_0/I with the concentration of Fe^{3+} in the range of 0–150 μM. (c) Dendrogram of different ions in hierarchical cluster analysis. (d) Hot plot of distances between different ions based on hierarchical cluster analysis. (e) Fluorescence responses of the **1**-based sensor under different interferences. (f) Lifetime decay curves of the **1**-based sensor under different concentrations of Fe^{3+} (Inset: the pie chart of PL lifetime at different concentrations of Fe^{3+}).

99.00%–100.18% with an RSD of 0.27%–0.94% in lake water, and 99.56%–101.78% with an RSD of 0.34%–1.23% in human serum were found, indicating that the developed sensor was viable for the quantitative detection of Fe^{3+} in real samples.

To figure out the sensing mechanism, the PL decay lifetime curves of **1** were recorded at 397 nm excitation peak and 620 nm emission peak, all obeying the mono-exponential function. The lifetimes of **1** showed a definite dependency on the concentration changes, which decreased drastically from 816.04 (0 μM) to 400.14 μs (400 μM) (Fig. 3f and Table S5†). This phenomenon suggests that dynamic quenching based on the collision between **1** and Fe^{3+} may play an important role in the Fe^{3+}-induced "ON–OFF" process. Generally, the quenching rate constant (K_q) can be obtained from the equation $K_{SV} = K_q\tau_0$ (τ_0 means the decay lifetime of **1** without Fe^{3+}), and the intermolecular collision frequency in a dynamic process is usually less than 2.0×10^{10} M^{-1} s^{-1}.[52] Here, τ_0 is 816.04 μs and the quenching rate constant (K_{SV}) is estimated to be 2.18×10^3 M^{-1} from the linear *S–V* function of $I_0/I = 0.992 + 0.00218[C_{Fe}]$, therefore K_q was calculated to be 2.67×10^6 M^{-1} s^{-1}. This value also confirms that the dynamic quenching pathway is predominant in Fe^{3+} detection. Moreover, the UV–vis spectrum of Fe^{3+} ion was recorded to further proclaim the quenching mechanism, which shows a broad absorption band (200–450 nm) centered around 297 nm. Clearly, the excitation spectrum of **1** exhibits large overlaps with the UV–vis absorption of Fe^{3+} ions, while the emission shows negligible overlap (Fig. S16†). This result precludes the fluorescence resonance energy transfer, but suggests the existence of competitive absorption.[53,54] That's to say, Fe^{3+} ions show strong competition with BBs or Eu^{3+} ions for light energy, which can weaken the excitation energy of BBs or Eu^{3+} ions, thus causing significant quenching.

Pyrophosphate ($P_2O_7^{4-}$, PPi) is the hydrolysis product of adenosine triphosphate, and is closely related to numerous fundamental chemical and biological processes such as DNA replication, cellular metabolism and enzymatic catalysis.[55,56] An adequate level of PPi can block calcification in blood plasma, synovial fluid and urine, exhibiting a vital effect on arthritis and chondrocalcinosis. Therefore, accurate detection of PPi is essential.[57,58] On account of the intense affinity of PPi towards metal ions causing emission quenching or enhancement, the resulting Fe^{3+}-quenched system might be a feasible way for recognizing PPi.

As illustrated in Fig. 4a and b, the emission intensity of Fe^{3+}-quenched system was progressively recovered with the continuous addition of PPi, and a recovery rate of about 78% was ultimately achieved when PPi concentration reached 800 μM. Thus, a bidirectional "ON–OFF–ON" PL sensing assay was developed for the successive detection of Fe^{3+} and PPi. To gain more insight into the relationship between emission intensity and analyte concentration, the PL enhancement coefficient (K_{EC}) was quantitatively analyzed from the equation $I_0/I = 1 + K_{EC}[C]$,[59] where [C] denotes the concentration of analyte, and I_0 and I are PL emission intensities without and with analyte, respectively. In the present system, the I/I_0 at 620 nm shows a good linear response to PPi with the equation of $I/I_0 = 1.0035 + 0.00282[C]$ over a wide concentration scope

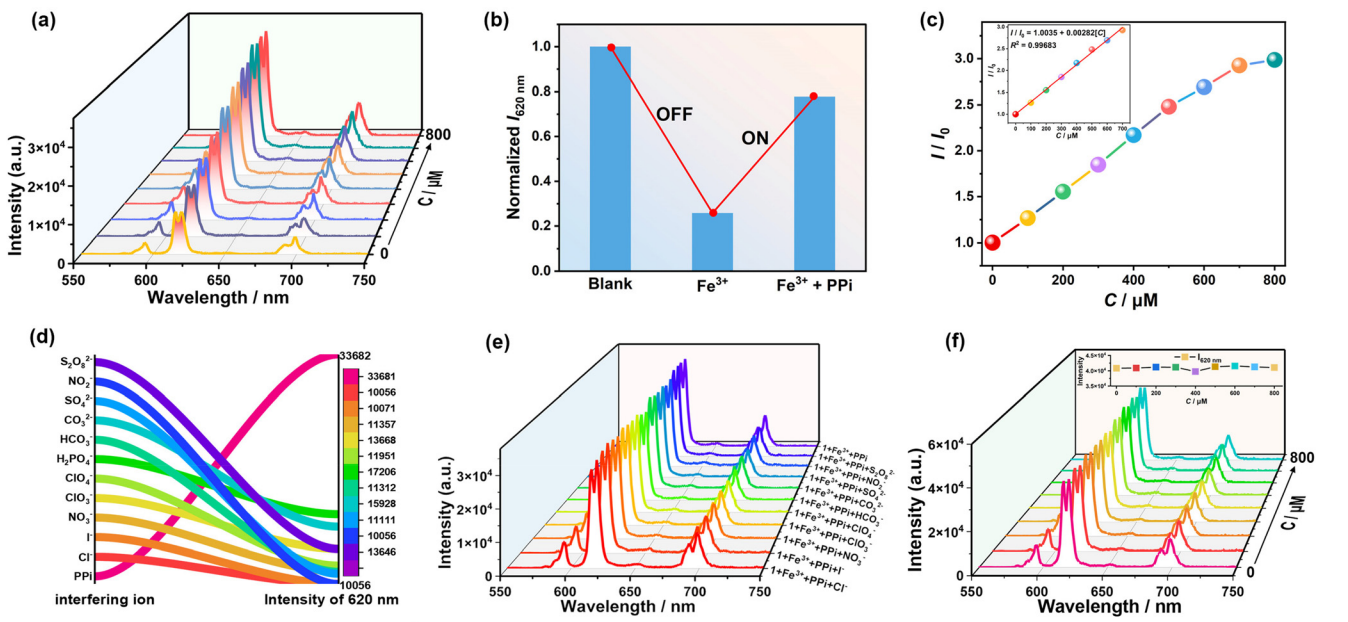

Fig. 4 (a) Evolution of the emission spectra of the Fe^{3+}-quenched system with different concentrations of PPi. (b) The variation of PL intensity during the whole ON–OFF–ON process. (c) Variation of I_0/I values at 620 nm of the Fe^{3+}-quenched system with the concentration of PPi (C_{Fe} = 400 μM). Inset: the linear variation of I_0/I with PPi concentration in the range of 0–700 μM. (d) Classification of different anions depending on their response patterns in the Fe^{3+}-quenched system. (e) Fluorescence responses of the Fe^{3+}-quenched system in the presence of PPi and other interfering anions. (f) Evolution of the emission spectra of the **1**-based sensor in different concentrations of PPi. (Inset: the PL intensity at 620 nm).

between 0 and 700 μM (Fig. 4c). The K_{EC} of the Fe^{3+}-quenched system for detecting PPi was found to be 2.82×10^3 M^{-1}, suggestive of the effective interaction between Fe^{3+} and PPi. The LOD of PPi was calculated to be 2.16 μM by the $3s/k$ rule (Table S6†), comparable to the previously reported sensors for detecting Fe^{3+} and PPi (Table S7†).

Next, the selectivity and anti-interference of Fe^{3+}-quenched system were studied by measuring its response to various anions including Cl^-, I^-, NO_3^-, ClO_3^-, ClO_4^-, HCO_3^-, CO_3^{2-}, SO_4^{2-}, NO_2^- and $S_2O_8^{2-}$ (Fig. 4d, e and S17†). These interfering anions induced very low recoveries in intensity of $^5D_0 \rightarrow {}^7F_2$ at the same concentrations of 800 μM, which was negligible in comparison with that of PPi. Besides, the recovery for PPi sensing was not affected by these interferents. Based on the good selectivity and anti-interference, the Fe^{3+}-quenched system can be established as a potential sensor for detecting PPi. Additionally, to exclude the potential impact of PPi on the **1**-based sensor, the PL evolution of the **1**-based sensor was recorded with the introduction of different concentrations of PPi. As exhibited in Fig. 4f, the impact of PPi on PL intensity was minimal, with PL intensity keeping steady even at concentrations up to 800 μM. As a consequence, the recovery of PL intensity is probably attributed to the affinity of Fe^{3+} towards PPi, and their combination greatly reduced the content of Fe^{3+} in the detection system, blocking the dynamic quenching process, thus the PL intensity of the Fe^{3+}-quenched system could be recovered. The PL lifetimes of the Fe^{3+}-quenched system with the addition of PPi were also investigated, which ultimately increased to 831.11 μs when PPi concentration was 800 μM (Fig. S18a, and Table S8†). As a comparison, the introduction of PPi alone into sensor **1** also caused the change in the lifetimes with a maximum up to 900 μs (Fig. S18b, and Table S9†), a bit higher than the initial lifetime of 816.04 μs of **1**, suggesting that PPi alone may also affect the recovery of PL lifetimes of the Fe^{3+}-quenched system apart from its combination with Fe^{3+}.

As another important criterion for evaluating sensor performance, the response times of sensor **1** towards Fe^{3+} and PPi were recorded. When Fe^{3+} (400 μM) was added into solution **1**, the emission intensity decreased immediately and quickly reached a plateau in less than 5 s (Fig. S19a†). By adding PPi (800 μM) into the above quenched system, the intensity dramatically increased and eventually achieved a stable level within 40 s (Fig. S19b†). These results manifest the response of **1** towards Fe^{3+} and the combination of Fe^{3+} with PPi are fast. Then the developed sensor was applied to detect Fe^{3+} and PPi in the serum to verify its applicability. Human serum was diluted 100-fold with deionized water, and **1** (2 mg mL^{-1}) was dissolved in the above serum. Then, a total of 400 μM Fe^{3+} was successively added to the **1**-containing serum to construct the Fe^{3+}-quenched luminescence system. The standard addition method was used in this system on subsequent addition of PPi. As manifested in Table S10,† recoveries of 99.69%–102.58% with RSDs of 0.56%–1.48% were found, indicating that the developed sensor has the effectiveness and practicality of detecting PPi in real samples.

Conclusions

In summary, a novel Bi–Te–Eu cluster embedded HPOT **1** has been fabricated, demonstrating the feasibility of combining HA pairs with Ln cations in the tungstate system to prepare mixed-HA-directed HPOTs. Particularly, the phenomenon that two types of HAs like a Bi–Te pair work together as linkers to grasp Ln and HPOT BBs has not been previously reported, and their tight connection modes endow **1** with excellent structural stability in water. Therefore, **1** was employed as a luminescence sensor to detect Fe^{3+} in water with remarkable selectivity, strong anti-interference ability and a low LOD (1.23 μM). This Fe^{3+}-quenched system was further applied to sensitively recognize PPi based on the strong affinity of Fe^{3+} and PPi, thus realizing a sequential detection system. This work highlights the vast potential of designing novel HPOTs directed by judiciously selected mixed-HA components and their promising applications in luminescence sensing in biological and environmental systems. More future efforts will be devoted to the controlled synthesis of poly-HA-templated HPOTs with higher structural complexity and functional properties.

Data availability

The data are available from the corresponding author on reasonable request.

Author contributions

Siyu Zhang and Tiantian Gong contributed equally to this work. They and Jiancai Liu performed the preparation, characterization, and photoluminescence sensing property determination and wrote the manuscript. Chenyun Liu, Qiuyu Wang and Fuxiu Chen participated in IR, TG, UV-vis spectroscopy and ESI-MS studies. Lijuan Chen and Junwei Zhao are responsible for proposing research ideas, determining crystal structures and revising the manuscript.

Conflicts of interest

There are no conflicts to declare.

Acknowledgements

This work was financially supported by the National Natural Science Foundations of China (22371066, 22101072, 22071042, and 22171070), Henan Science and Technology Research Project (242102231046), China Postdoctoral Science Foundation (2021M701067), the Program for Kaifeng Innovation Teams of Science and Technology, and the Key Project of the Youth Interdisciplinary Foundation of Henan University.

References

1 Z. Wang, Y.-J. Zhu, B.-L. Han, Y.-Z. Li, C.-H. Tung and D. Sun, A route to metalloligands consolidated silver nanoclusters by grafting thiacalix[4]arene onto polyoxovanadates, *Nat. Commun.*, 2023, **14**, 5295.

2 J.-J. Li, C.-Y. Liu, Z.-J. Guan, Z. Lei and Q.-M. Wang, Anion-directed regulation of structures and luminescence of hetero-metallic clusters, *Angew. Chem., Int. Ed.*, 2022, **61**, e202201549.

3 W. Huang, W. Chen, Q. Bai, Z. Zhang, M. Feng and Z. Zheng, Anion-guided stepwise assembly of high-nuclearity lanthanide hydroxide clusters, *Angew. Chem., Int. Ed.*, 2022, **61**, e202205385.

4 Y. Q. Feng, F. Y. Fu, L. L. Zeng, M. Y. Zhao, X. Xin, J. K. Liang, M. Zhou, X. K. Fang, H. J. Lv and G.-Y. Yang, Atomically precise silver clusters stabilized by lacunary polyoxometalates with photocatalytic CO_2 reduction activity, *Angew. Chem., Int. Ed.*, 2024, **63**, e202317341.

5 Z. M. Wang, X. Xin, M. Zhang, Z. Li, H. J. Lv and G.-Y. Yang, Recent advances of mixed-transition-metal-substituted polyoxometalates, *Sci. China: Chem.*, 2022, **65**, 1515.

6 M. Zhang, H. J. Li, J. H. Zhang, H. J. Lv and G. Y. Yang, Research advances of light-driven hydrogen evolution using polyoxometalate- based catalysts, *Chin. J. Catal.*, 2021, **42**, 855.

7 M. H. Zhu, T. Iwano, M. J. Tan, D. Akutsu, S. Uchida, G. Y. Chen and X. K. Fang, Macrocyclic polyoxometalates: Selective polyanion binding and ultrahigh proton conduction, *Angew. Chem., Int. Ed.*, 2022, **61**, e202200666.

8 R. Ge, X.-X. Li and S.-T. Zheng, Recent advances in polyoxometalate-templated high-nuclear silver clusters, *Coord. Chem. Rev.*, 2021, **435**, 213787.

9 X.-M. Luo, Y.-K. Li, X.-Y. Dong and S.-Q. Zang, Platonic and Archimedean solids in discrete metal-containing clusters, *Chem. Soc. Rev.*, 2023, **52**, 383.

10 A. Parrot, A. Bernard, A. Jacquart, S. A. Serapian, C. Bo, E. Derat, O. Oms, A. Dolbecq, A. Proust, R. Metivier, P. Mialane and G. Izzet, Photochromism and dual-color fluorescence in a polyoxometalate benzospiropyran molecular switch, *Angew. Chem., Int. Ed.*, 2017, **56**, 4872.

11 Q. D. Liu, Q. H. Zhang, W. X. Shi, H. S. Hu, J. Zhuang and X. Wang, Self-assembly of polyoxometalate clusters into two-dimensional clusterphene structures featuring hexagonal pores, *Nat. Chem.*, 2022, **14**, 433.

12 M. J. W. Budych, K. Staszak, A. Bajek, F. Pniewski, R. Jastrząb, M. Staszak, B. Tylkowski and K. Wieszczycka, The future of polyoxymetalates for biological and chemical applications, *Coord. Chem. Rev.*, 2023, **493**, 215306.

13 J. Zhao, K. X. Li, K. W. Wan, T. D. Sun, N. N. Zheng, F. J. Zhu, J. C. Ma, J. Jiao, T. C. Li, J. Y. Ni, X. H. Shi, H. Wang, Q. Peng, J. Ai, W. H. Xu and S. Q. Liu, Organoplatinum-substituted polyoxometalate inhibits β-amyloid aggregation for Alzheimer's therapy, *Angew. Chem., Int. Ed.*, 2019, **58**, 18032.

14 Z.-X. Yang, F. Gong, D. M. Lin and Y. Huo, Recent advances in polyoxometalate-based single-molecule magnets, *Coord. Chem. Rev.*, 2023, **492**, 215205.

15 H. Y. Zhang, W.-L. Zhao, H. Q. Li, Q. H. Zhuang, Z. Q. Sun, D. Y. Cui, X. J. Chen, A. Guo, X. Ji, S. An, W. Chen and Y.-F. Song, Latest progress in covalently modified polyoxometalates-based molecular assemblies and advanced materials, *Polyoxometalates*, 2022, **1**, 9140011.

16 S. J. Li, Y. F. Zhou, N. N. Ma, J. Zhang, Z. P. Zheng, C. Streb and X. N. Chen, Organoboron-functionalization enables the hierarchical assembly of giant polyoxometalate nanocapsules, *Angew. Chem., Int. Ed.*, 2020, **59**, 8537.

17 V. Das, R. Kaushik and F. Hussain, Heterometallic 3d-4f polyoxometalates: An emerging field with structural diversity to multiple applications, *Coord. Chem. Rev.*, 2020, **143**, 213271.

18 J.-C. Liu, J.-W. Zhao, C. Streb and Y.-F. Song, Recent advances on high-nuclear polyoxometalate clusters, *Coord. Chem. Rev.*, 2022, **471**, 214734.

19 C. M. Granadeiro, D. Julião, S. O. Ribeiro, L. Cunha-Silva and S. S. Balula, Recent advances in lanthanide-coordinated polyoxometalates: From structural overview to functional materials, *Coord. Chem. Rev.*, 2023, **476**, 214914.

20 P. T. Ma, F. Hu, J. P. Wang and J. Y. Niu, Carboxylate covalently modified polyoxometalates: From synthesis, structural diversity to applications, *Coord. Chem. Rev.*, 2019, **378**, 281.

21 Z. Li, Z.-H. Lv, H. Yu, Y.-Q. Sun, X.-X. Li and S.-T. Zheng, Polyoxotungstate nanoclusters with exceptional proton-conducting and luminescent properties, *CCS Chem.*, 2022, **4**, 2938.

22 F. Hussain, R. W. Gable, M. Speldrich, P. Kögerler and C. Boskovic, Polyoxotungstate-encapsulated Gd_6 and Yb_{10} complexes, *Chem. Commun.*, 2009, 328.

23 J. Yan, D.-L. Long and L. Cronin, Development of a building block strategy to access gigantic nanoscale heteropolyoxo- tungstates by using SeO_3^{2-} as a template linker, *Angew. Chem., Int. Ed.*, 2010, **49**, 4117.

24 J. Gao, J. Yan, S. G. Mitchell, H. N. Miras, A. G. Boulay, D.-L. Long and L. Cronin, Self-assembly of a family of macrocyclic polyoxotungstates with emergent material properties, *Chem. Sci.*, 2011, **2**, 1502.

25 W.-C. Chen, H.-L. Li, X.-L. Wang, K.-Z. Shao, Z.-M. Su and E.-B. Wang, Assembly of cerium(III)-stabilized polyoxotungstate nanoclusters with SeO_3^{2-}/TeO_3^{2-} templates: From single polyoxoanions to inorganic hollow spheres in dilute solution, *Chem. – Eur. J.*, 2013, **19**, 11007.

26 X.-B. Han, Z.-M. Zhang, T. Zhang, Y.-G. Li, W. Lin, W. You, Z.-M. Su and E.-B. Wang, Polyoxometalate-based cobalt phosphate molecular catalysts for visible light-driven water oxidation, *J. Am. Chem. Soc.*, 2014, **136**, 5359.

27 L. L. Li, H. Y. Han, Y. H. Wang, H. Q. Tan, H. Y. Zang and Y. G. Li, Construction of polyoxometalates from dynamic lacunary polyoxotungstate building blocks and lanthanide linkers, *Dalton Trans.*, 2015, **44**, 11429.

28 B. Artetxe, S. Reinoso, L. S. Felices, L. Lezama, J. M. Gutiérrez- Zorrilla, C. Vicent, F. Haso and T. B. Liu,

New perspectives for old clusters: Anderson–Evans anions as building blocks of large polyoxometalate frameworks in a series of heterometallic 3d–4f species, *Chem. – Eur. J.*, 2016, **22**, 4616.

29 J. Cai, X.-Y. Zheng, J. Xie, Z.-H. Yan, X.-J. Kong, Y.-P. Ren, L.-S. Long and L.-S. Zheng, Anion-dependent assembly of hetero-metallic 3d–4f clusters based on a lacunary polyoxometalate, *Inorg. Chem.*, 2017, **56**, 8439.

30 H.-P. Xiao, Y.-S. Hao, X.-X. Li, P. Xu, M.-D. Huang and S.-T. Zheng, A water-soluble antimony-rich polyoxometalate with broad spectrum antitumor activities, *Angew. Chem., Int. Ed.*, 2022, **61**, e202210019.

31 K. Cui, F. Li, L. Xu, B. Xu, N. Jiang, Y. Wang and J. Zhang, Lanthanide–tungstobismuthate clusters based on $[BiW_9O_{33}]^{9-}$ building units: Synthesis, crystal structures, luminescent and magnetic properties, *Dalton Trans.*, 2012, **41**, 4871.

32 J.-C. Liu, Q. Han, L.-J. Chen, J.-W. Zhao, C. Streb and Y.-F. Song, Aggregation of giant cerium–bismuth tungstate clusters into a 3d porous framework with high proton conductivity, *Angew. Chem., Int. Ed.*, 2018, **57**, 8416.

33 S. Maeda, T. Goto, M. Takamoto, K. Eda, S. Himeno, H. Takahashi and T. Hori, An approach to the synthesis of polyoxometalate encapsulating different kinds of oxoanions as heteroions: Bisphosphitopyrophosphatotri-acontamolybdate $[(HPO_3)_2(P_2O_7)\text{-}Mo_{30}O_{90}]^{8-}$, *Inorg. Chem.*, 2008, **47**, 11197.

34 T. T. Gong, J. Jiang, S. Yang, J. C. Liu, L. J. Chen and J. W. Zhao, Lanthanide-incorporated polyoxometalates assembled from mixed-heteroatom-oriented three-layered cage clusters, *Inorg. Chem.*, 2022, **61**, 18147.

35 X. D. Jia, Z. G. Tang, L. N. Meng, Z. X. Wang, D. Wang, L. J. Chen and J. W. Zhao, Cerium-encapsulated SbIII–SeIV-templating polyoxotungstate for electrochemically sensing human multidrug resistance gene segment, *Inorg. Chem.*, 2023, **62**, 13639.

36 Q. Zheng, L. Vilà-Nadal, Z. Lang, J.-J. Chen, D.-L. Long, J. S. Mathieson, J. M. Poblet and L. Cronin, Self-sorting of heteroanions in the assembly of cross-shaped polyoxometalate clusters, *J. Am. Chem. Soc.*, 2018, **140**, 2595.

37 T. T. Cui, L. Qin, F. Y. Fu, X. Xin, H. J. Li, X. K. Fang and H. J. Lv, Pentadecanuclear Fe-containing polyoxometalate catalyst for visible-light-driven generation of hydrogen, *Inorg. Chem.*, 2021, **60**, 4124.

38 M.-Y. Yao, Y.-F. Liu, X.-X. Li, G.-P. Yang and S.-T. Zheng, The largest Se-4f cluster incorporated polyoxometalate with high Lewis acid–base catalytic activity, *Chem. Commun.*, 2022, **58**, 5737.

39 A. Haider, B. S. Bassil, J. Soriano-López, H. M. Qasim, C. S. de Pipaón, M. Ibrahim, D. Dutta, Y.-S. Koo, J. J. Carbó, J. M. Poblet, J. R. Galán-Mascarós and U. Kortz, 9-Cobalt (II)-containing 27-tungsto-3-germanate(IV): Synthesis, structure, computational modeling, and heterogeneous water oxidation catalysis, *Inorg. Chem.*, 2019, **58**, 11308.

40 S.-R. Li, H.-Y. Wang, H.-F. Su, H.-J. Chen, M.-H. Du, L.-S. Long, X.-J. Kong and L.-S. Zheng, A giant 3d-4f polyoxometalate super-tetrahedron with high proton conductivity, *Small Methods*, 2020, 2000777.

41 X.-B. Han, Y.-G. Li, Z.-M. Zhang, H.-Q. Tan, Y. Lu and E.-B. Wang, Polyoxometalate-based nickel clusters as visible light-driven water oxidation catalysts, *J. Am. Chem. Soc.*, 2015, **137**, 5486.

42 S. Yang, T. T. Gong, Y. D. Dai, X. X. Xiao, J. C. Liu, L. J. Chen and J. W. Zhao, An unusual bismuth–antimony–europium cluster-imbedded polyoxotungstate and its bidirectional luminescence detection, *Inorg. Chem.*, 2023, **62**, 17861.

43 C. Lian, H.-L. Li and G.-Y. Yang, A μ-AsO_4-bridging hexadeca-nuclear Ni-substituted polyoxotungstate, *Inorg. Chem.*, 2021, **60**, 3996.

44 Y. Zhao, X. Zhai, L. Shao, L. Li, Y. Liu, X. Zhang, J. Liu, F. Meng and Y. Fu, An ultra-high quantum yield Tb-MOF with phenolic hydroxyl as the recognition group for a highly selective and sensitive detection of Fe^{3+}, *J. Mater. Chem. C*, 2021, **9**, 15840.

45 J. Qian, N. Huang, Q. Lu, C. Wen and J. Xia, A novel D-A-D-typed rod-like fluorescent material for efficient Fe(III) and Cr(IV) detection: Synthesis, structure and properties, *Sens. Actuators, B*, 2020, **320**, 128377.

46 P. S. Nayab and M. Shkir, Rapid and simultaneous detection of Cr(III) and Fe(III) ions by a new naked eye and fluorescent probe and its application in real samples, *Sens. Actuators, B*, 2017, **251**, 951.

47 N. Narayanaswamy and T. Govindaraju, Aldazine-based colorimetric sensors for Cu^{2+} and Fe^{3+}, *Sens. Actuators, B*, 2012, **161**, 304.

48 L. Guo, Y. Liu, R. Kong, G. Chen, Z. Liu, F. Qu, L. Xia and W. Tan, A metal–organic framework as selectivity regulator for Fe^{3+} and ascorbic acid detection, *Anal. Chem.*, 2019, **91**, 12453.

49 Y. Zhang and B. Yan, MIL-61 and Eu^{3+}@MIL-61 as signal transducers to construct an intelligent boolean logical library based on visualized luminescent metal–organic frameworks, *ACS Appl. Mater. Interfaces*, 2019, **11**, 20125.

50 D. Dinda, A. Gupta, B. K. Shaw, S. Sadhu and S. K. Saha, Highly selective detection of trinitrophenol by luminescent functionalized reduced graphene oxide through FRET mechanism, *ACS Appl. Mater. Interfaces*, 2014, **6**, 10722.

51 A. M. Committee, Recommendations for the definition, estimation and use of the detection limit, *Analyst*, 1987, **112**, 199.

52 Z.-H. Jiao, S.-L. Hou, X.-M. Kang, X.-P. Yang and B. Zhao, Recyclable luminescence sensor for dinotefuran in water by stable cadmium–organic framework, *Anal. Chem.*, 2021, **93**, 6599.

53 K. Vellingiri, D. W. Boukhvalov, S. K. Pandey, A. Deep and K.-H. Kim, Luminescent metal–organic frameworks for the detection of nitrobenzene in aqueous media, *Sens. Actuators, B*, 2017, **245**, 305.

54 Z. S. Han, K. Y. Wang, Y. L. Chen, J. N. Li, S. J. Teat, S. H. Yang, W. Shi and P. Cheng, A multicenter metal–organic framework for quantitative detection of multicomponent organic mixtures, *CCS Chem.*, 2022, **4**, 3238.

55 J.-J. Tsa, Y.-C. Zhan, Y.-Y. Wu and Y.-C. Chen, A facile switch-on fluorescence sensing method for detecting phosphates from complex aqueous samples, *Sens. Actuators, B*, 2023, **380**, 133298.
56 J. Zhao, S. Wang, S. Lu, J. Sun and X. Yang, A luminescent europium-dipicolinic acid nanohybrid for the rapid and selective sensing of pyrophosphate and alkaline phosphatase activity, *Nanoscale*, 2018, **10**, 7163.
57 X. Xu, D. Ren, Y. Chai, X. Cheng, J. Mei, J. Bao, F. Wei, G. Xu, Q. Hu and Y. Cen, Dual-emission carbon dots-based fluorescent probe for ratiometric sensing of Fe(III) and pyrophosphate in biological samples, *Sens. Actuators, B*, 2019, **298**, 126829.
58 F. Wang, C. Zhang, Q. Xue, H. Li and Y. Xian, Label-free upconversion nanoparticles-based fluorescent probes for sequential sensing of Cu^{2+}, pyrophosphate and alkaline phosphatase activity, *Biosens. Bioelectron.*, 2017, **95**, 21.
59 M. Wang, L. Guo and D. P. Cao, Amino-functionalized luminescent metal–organic framework test paper for rapid and selective sensing of SO_2 gas and its derivatives by luminescence turn-on effect, *Anal. Chem.*, 2018, **90**, 3608.